

Article

Influence of Ti Substitution on Electrochemical Performance and Evolution of $\text{LiMn}_{1.5-x}\text{Ni}_{0.5}\text{Ti}_x\text{O}_4$ ($x = 0.05, 0.1, 0.3$) as a High Voltage Cathode Material with a Very Long Cycle Life

Svetlana Niketic ¹, Chae-Ho Yim ¹ , Jigang Zhou ² , Jian Wang ²  and Yaser Abu-Lebdeh ^{1,*}

¹ National Research Council of Canada, Energy, Mining and Environment Research Centre, 1200 Montreal Road, Ottawa, ON K1A 0R6, Canada; Svetlana.Niketic@nrc-cnrc.gc.ca (S.N.); Chae-Ho.Yim@nrc-cnrc.gc.ca (C.-H.Y.)

² Canadian Light Source Incorporation, Saskatoon, SK S7N 2V3, Canada; jigang.zhou@lightsource.ca (J.Z.); jian.wang@lightsource.ca (J.W.)

* Correspondence: Yaser.Abu-Lebdeh@nrc-cnrc.gc.ca; Tel.: +1-613-949-4184; Fax: +1-613-991-2384

Abstract: The high voltage spinel material $\text{LiMn}_{1.5}\text{Ni}_{0.5}\text{O}_4$ (LMNO) has the potential to increase the energy density of lithium batteries. However, its battery performance suffers from poor long-term cycling and high-temperature stability. In order to overcome these limitations, we have studied the effect of partial substitution of Mn with Ti and $\text{LiMn}_{1.5-x}\text{Ni}_{0.5}\text{Ti}_x\text{O}_4$ ($x = 0.05, 0.1, 0.3$), LMNTO, materials have been synthesized in a newly modified sol-gel method and then characterized by TEM, SEM (EDX), AC Electrochemical Impedance Spectroscopy and Soft X-ray Spectromicroscopy. We have demonstrated that the long-term cycling limitation with these types of materials can be resolved and herein 2000 cycles at a high C-rate have been demonstrated in half cells. We have attributed this behavior to a possible charge compensation mechanism as evidenced by a Soft X-ray Spectromicroscopy study of delithiated LMNTO materials. This work takes high energy density batteries based on high voltage spinel material one step further towards commercialization, and it is believed that further improvement can be achieved using new electrolyte formulations.

Keywords: Li-ion; battery; energy storage; high-potential; cathode; spinel oxide



Citation: Niketic, S.; Yim, C.-H.; Zhou, J.; Wang, J.; Abu-Lebdeh, Y. Influence of Ti Substitution on Electrochemical Performance and Evolution of $\text{LiMn}_{1.5-x}\text{Ni}_{0.5}\text{Ti}_x\text{O}_4$ ($x = 0.05, 0.1, 0.3$) as a High Voltage Cathode Material with a Very Long Cycle Life. *Inorganics* **2022**, *10*, 10. <https://doi.org/10.3390/inorganics10010010>

Academic Editors: Christian Julien and Alain Mauger

Received: 16 December 2021

Accepted: 7 January 2022

Published: 12 January 2022

Publisher's Note: MDPI stays neutral with regard to jurisdictional claims in published maps and institutional affiliations.



Copyright: © 2022 by the authors. Licensee MDPI, Basel, Switzerland. This article is an open access article distributed under the terms and conditions of the Creative Commons Attribution (CC BY) license (<https://creativecommons.org/licenses/by/4.0/>).

1. Introduction

Although lithium-ion batteries are currently the dominant power source for many mobile and stationary applications such as consumer electronics, power tools, electric vehicles and electrical grid, there is an ever-increasing demand to further increase the energy and power densities, extend cycle life, enhance safety and lower their cost. One approach to improve the energy density is to increase the operating voltage of the batteries by developing high voltage “positive” cathode materials in combination with the low voltage, conventional graphite anode. However, such a development would have the added benefit of facilitating the use of safer, higher voltage anode materials such as $\text{Li}_4\text{Ti}_5\text{O}_{12}$ for a safer Li-ion cell with practical voltage (>3 V). The spinel $\text{LiMn}_{1.5}\text{Ni}_{0.5}\text{O}_4$, LMNO, cathode material has been identified as a promising candidate since the discovery that the substitution of the parent spinel LiMn_2O_4 with Ni from Mn cations shifts the potential of the redox reaction from 4.1 V vs. Li/Li⁺ related to Mn^{+3/+4} redox couple to 4.7 V vs. Li/Li⁺ related to Ni^{+2/+4} couple. Similarly substituted spinels with different metal cations have also been reported, $\text{LiMn}_{2-x}\text{M}_x\text{O}_4$ (M = Cr, Co, Fe, Ni, Cu), and also show high potential above 4.5 V [1–7]. Among the most promising candidates is $\text{LiMn}_{1.5}\text{Ni}_{0.5}\text{O}_4$, which is proven to exhibit close to theoretical discharge capacity (148 mAh g^{−1}) at around 4.7 V [8–12]. A wide variety of preparation methods for synthesizing the above material have been described over the years such as solid-state [1,9,12–15], sucrose-aided combustion [16,17], combinational annealing process [18], molten salts [19], ultrasonic spray pyrolysis [20], electrostatic spray deposition [10], pulsed laser deposition [15], mechanochemical [2,21],

coprecipitations [11,22], precipitation [7] and sol-gel synthesis [1,3,6,8,9,12,23–26]. In a recent review, Yi et al. [22] have summarized the possible failure modes of $\text{LiNi}_{0.5}\text{Mn}_{1.5}\text{O}_4$ and the key strategies for enhancing the battery performance. It was demonstrated by many research groups that long-term cycling especially at higher temperature and rate capability is the main issue. Possible approaches are modified synthetic methods to obtain preferred crystals (platelet over octahedron), surface coatings with metal oxides or carbon and substitution (doping) with other elements that might improve the structural and/or electrochemical stability.

It has been suggested that partial substitution of Mn^{4+} with Ti^{4+} could improve cycle life, the reversible capacity and capacity retention²⁶ due to changes in the chemistry of the structure as a result of the shorter and stronger Ti-O bonds and the suppression of Ni/Mn ordering which increases the Li-ion diffusion rate [27–29]. Alcantara et al. [28] reported that the doping of small amounts of Ti improved the electrochemical performance whereas deterioration of the reversible capacity was observed for large amounts of Ti. Jin et al. [29] reported that carbon-coated $\text{LiMn}_{1.5}\text{Ni}_{0.4}\text{Ti}_{0.1}\text{O}_4$ exhibited better excellent cycling stability, higher discharge capacity and coulombic efficiency compared to the LMNO and for $\text{LiMn}_{1.5}\text{Ni}_{0.4}\text{Ti}_{0.1}\text{O}_4$ samples at 55 °C. Kim et al. [30] reported that $\text{LiMn}_{1.5-x}\text{Ni}_{0.5}\text{Ti}_x\text{O}_4$ ($0.2 \leq x \leq 0.4$) in half and full-cells coupled with either graphite or $\text{Li}_4\text{Ti}_5\text{O}_{12}$ negative electrodes showed higher discharge capacities and cycling stabilities than those of $\text{Li}_4\text{Ti}_5\text{O}_{12}$ /LMNO full-cell at room temperature and 45°, but still show the noticeable capacity fade at 45 °C because of electrolyte decomposition. Höweling et al. [31] also reported Ti-doped graphite/LNMO cells experiencing a lower but still severe loss of capacity due to the loss of active lithium during cycling. Table 1 summarizes all the physical characteristics obtained for Ti-doped LMNO.

Table 1. Summary of Ti-doped LMNO, $\text{LiMn}_{1.5-x}\text{Ni}_{0.5}\text{Ti}_x\text{O}_4$, reported in the literature with battery performance as a function of a synthetic method, electrolyte type and temperature.

Ref	x	Synthesis Method	Electrolyte	Full Cell	Long Term Cycling	Temperature
[27]	<0.6	Solid-state	EC: DMC	-	100	60 °C
[28]	0.05–0.6 (battery test 0.05, 0.2)	Precipitation	EC:DEC	-	<5	-
[29]	0.1 (Carbon coating)	Solid-state	EC:DMC	-	<1000	55 °C
[30]	0.3	Solid-state	EC:EMC	Graphite/LMNO LTO/LMNO	<200	45 °C
[31]	0.02	Spray pyrolysis	EC:DMC	Graphite/LMNO	<200	25 °C 25 °C
THIS WORK	0.1	Modified sol-gel	EC:DMC EC:DEC	LTO/LMNO	>2000	60 °C 25 °C 60 °C

As shown in the table, the sol-gel method has not been previously used to synthesize $\text{LiMn}_{1.5-x}\text{Ni}_{0.5}\text{Ti}_x\text{O}_4$ materials. The use of the sol-gel method offers many advantages over other conventional methods such as solid-state and co-precipitation; lowering reaction temperature, better mixing to ensure homogeneous distribution of dopant Ti ions in the reaction mixture and enable smaller particle size.

In this work, we report results on the spinel materials $\text{LiMn}_{1.5}\text{Ni}_{0.5}\text{O}_4$ and $\text{LiMn}_{1.5-x}\text{Ni}_{0.5}\text{Ti}_x\text{O}_4$ ($x = 0.05, 0.1, 0.3$) obtained from a newly modified sol-gel synthetic method with the electrochemically preferred crystalline structure and shape. The materials were characterized and tested in half and full cells and battery results show high discharge capacities and very long cycle life that extend to over 2000 cycles in both half and full cells, demonstrating the benefit of Ti addition. Furthermore, basic and advanced characterization helped shed light on a possible mechanism for the enhanced performance. The results indicate that this

material has the potential to increase the energy density of lithium batteries while retaining a long cycle life.

2. Experimental

The synthetic method used was a slight variation of a sol-gel method described in Amine et al. [1], Wu and Kim [8] and Zhong et al. [9]. $\text{LiMn}_{1.5}\text{Ni}_{0.5}\text{O}_4$ was prepared from a stoichiometric mixture of manganese acetate tetrahydrate (Aldrich, Oakville, ON, Canada), nickel nitrate hexahydrate (Aldrich, Oakville, ON, Canada) and lithium hydroxide monohydrate (Anachemia, Montreal, QC, Canada), dissolved in distilled water. After the addition of a small amount of carbon black, the pH of the solution was adjusted using ammonium hydroxide to pH 9–9.5. The resulting mixture was stirred for 1 h at room temperature, before heating at 80 °C to form a viscous gel. This gel was then fired in the air at 850 °C for 12 h and subsequently annealed at 600 °C for 24 h, followed by rapid cooling. The synthesis of Ti substituted $\text{LiMn}_{1.5}\text{Ni}_{0.5}\text{O}_4$ was the same except that +nickel acetate tetrahydrate (Aldrich) was used as a reactant as opposed to nickel nitrate hexahydrate and the pH was adjusted to 10. Moreover, different amounts of Ti in the form of ammonium titanyl oxalate (Aldrich) were added to the precursors' mixture. Powder samples fired were analyzed by flame atomic absorption spectroscopy (AAS) for Li, Mn and Ni content after dissolving in dilute nitric acid. Further analysis of the samples was performed by scanning electron microscopy (SEM), transmission electron microscopy (TEM), powder X-ray diffraction (XRD) and galvanostatic techniques. Micrographs were collected from three different locations on the powder and electrode surfaces using a JEOL 840 A SEM with an accelerating voltage of 20 kV and a working distance of 15 mm. TEM micrographs were obtained with a Philips CM20 microscope (Philips, Amsterdam, Netherlands) operating at a voltage of 200 kV. The powder samples were dispersed in alcohol, and one to two drops of dispersion was transferred to a carbon-coated, 400 mesh copper grid, and allowed to dry before measurements. Powder X-ray diffraction was carried out on a sample in a silicon zero-background holder with two different Bruker-AXS D8 (Bruker, Leipzig, Germany) diffractometers using Cu $K\alpha$ or Cr $K\alpha$. The first was a twin-mirror parallel beam system used between 10–90° 2θ with a step size of 0.03° and a 2 s count time. Initial results suggested that there may be shoulders on some of the peaks, so a second scan using a second, higher resolution Bruker-AXS D8 instrument equipped with a Vantec PSD detector from 15 up to 140° 2θ was carried out in an attempt to separate any closely related phases. The diffractometer configuration used on the second diffractometer was a 10° PSD detector window, 0.2° divergence slit, radial Soller slits, 0.0142° step size and 5 s count time. The detector discriminators were adjusted to filter out most of the fluorescence from the manganese. The resulting patterns were analyzed with the Pawley [32] and Rietveld [33] methods using the TOPAS 4 beta software from Bruker-AXS. To reduce correlations with the overlapping reflections, an overall isotropic displacement parameter (B_{iso}) was used for the different spinel structures. The scattering factors of Mn and Ni are too close to distinguish them from a single X-ray diffraction pattern, so the results are described in terms of transition metal (TM) occupancy.

STXM was performed at the SM beamline of Canadian Light Source (CLS). The active particles were released from a small piece cut of the electrode by ultrasonication with methanol. A drop of the dispensation was deposited onto a Si₃N₄ window and allowed to dry before STXM. The SM STXM is equipped with a 25 nm outermost-zone zone plate (CXRO, Berkeley Lab, Berkeley, CA, USA), and the diffraction-limited spatial resolution for this zone plate is 30 nm. A 500 L/mm plane grating monochromator (PGM) was used for O K-edge and Ti, Ni L₃-edge measurements. The image pixel size was 25 nm with a 1 ms dwell time per pixel. X-ray photon energy was calibrated using XANES of CO₂ reported in the literature. A circularly polarized soft X-ray beam from the SM EPU was used to average out the in-plane polarization dependence of X-ray absorption if there is any such effect.

Electrochemical testing was carried out using 2325-type coin cells assembled in an argon-filled glovebox. The electrode material was made by mixing 76 wt% $\text{LiMn}_{1.5}\text{Ni}_{0.5}\text{O}_4$,

7 wt% KS-4 graphite (Lonza, Basel, Switzerland), 7 wt% Super S carbon (Timcal, Bodio, Switzerland) and 10 wt% PVDF(Kynar) binder in *N*-methyl-pyrrolidone (NMP) (Sigma-Aldrich, St. Louis, MO, USA). For $\text{LiMn}_{1.5-x}\text{Ni}_{0.5}\text{Ti}_x\text{O}_4$ ($x = 0.05, 0.1, 0.3$) samples of active material, KS-4 graphite, Super S carbon and PVDF binder in NMP were adjusted to (63:12:13:12 wt%). The electrodes were formed by spreading slurry onto high purity aluminum foil using a doctor blade. After drying overnight in an oven at 85 °C, individual 12.5 mm diameter electrodes were punched out and pressed under a pressure of 0.5 t. Electrodes were transferred to a vacuum oven at 90 °C for further drying. Lithium metal foil was used as the anode in half-cell testing and 1 M LiPF_6 in (3:7 Ethylene carbonate: Diethyl carbonate) was used as the electrolyte. Microporous propylene separators (Celgard 2500, Celgard, Charlotte, NC, USA) were used between cathode and anode. All components and hardware coin cells parts were assembled in an Argon-filled Glove Box. Galvanostatic cycling was carried out using both custom-built Felton and commercial Arbin cyclers at different current rates (22, 88, 176, 300 and 675 mAh/g) and cycling rates from 0.16 C to 5 C and over a voltage range of 3.5–4.9 V at room temperature and 60 °C.

3. Results and Discussion

3.1. Characterization of LMNO and LMNTO Materials

The Unsubstituted $\text{LiMn}_{1.5}\text{Ni}_{0.5}\text{O}_4$ Cathode Material

The unsubstituted $\text{LiMn}_{1.5}\text{Ni}_{0.5}\text{O}_4$ cathode material was prepared by the modified sol-gel method and a black powder was obtained. Chemical analysis of the powder by Atomic Absorption showed that the stoichiometry of the sample preparation is $\text{Li}_{1.08}\text{Mn}_{1.49}\text{Ni}_{0.51}\text{O}_{4.17}$, very close to the expected theoretical stoichiometry. Figure 1a shows an SEM image of the $\text{LiMn}_{1.5}\text{Ni}_{0.5}\text{O}_4$ powder, which appears to have a uniform, mono-modal particle size distribution composed of distinct octahedron crystal facets with an average of 2 μm (microns) edge length. The Rietveld difference plot for the sample is shown in the XRD patterns in Figure 1b. The refinement revealed the presence of 88 wt% pure phase, 9 wt% Ni-deficient phase and 3% nickel oxide as a minor impurity that is probably related to the nickel solubility limit for this type of materials.

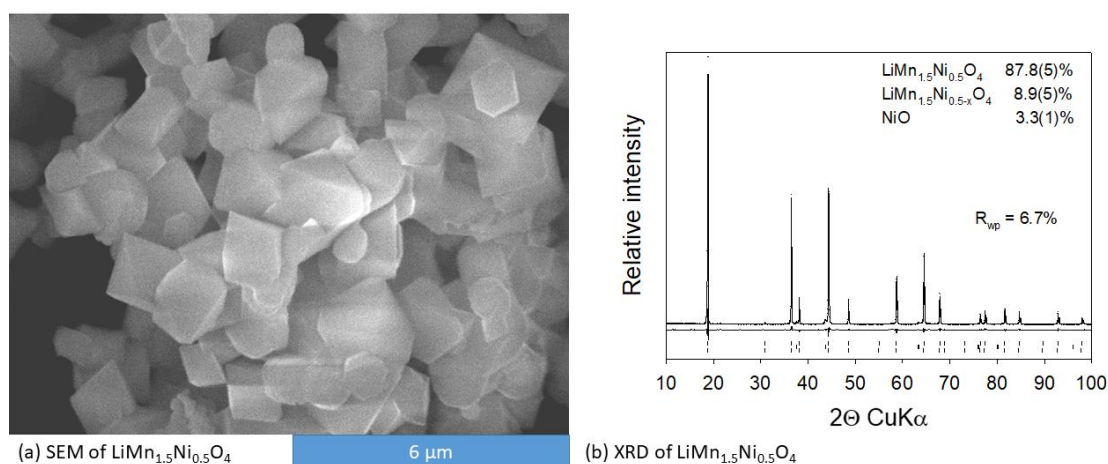


Figure 1. (a) SEM image and (b) XRD pattern of synthesized LMNO material.

3.2. Ti Substitution of $\text{LiMn}_{1.5}\text{Ni}_{0.5}\text{O}_4$ Cathode Material

The Ti substituted $\text{LiMn}_{1.5}\text{Ni}_{0.5}\text{O}_4$ cathode materials were prepared by the same modified sol-gel method with the amount of Ti, x , varying from 0.05 to 0.3. Figure 2a shows an SEM image of the 0.1 Ti substituted $\text{LiMn}_{1.5}\text{Ni}_{0.4}\text{Ti}_{0.1}\text{O}_4$ powder. The sample appears to have a uniform, mono-modal particle size distribution composed of octahedron crystal facets such as morphologies with a 2 μm edge length similar to the unsubstituted LMNO. TEM images of the sample, Figure 2b, were taken along with EDX which confirmed the presence of Ti in the crystallites. XRD results in Figure 3 show that there is a minor

impurity of a Ni-rich oxide which is probably Ni_6MnO_8 . Moreover, there is no evidence in Rietveld's analysis of ordered $\text{P4}_3\text{32}$ structure–spinel phases appear to be disordered Fd-3m structure as evidenced by the lack of 011 reflections at $15.4\ 2\theta$ of the $\text{P4}_3\text{32}$ ordered cell in the substituted samples laid over the calculated reflections in the inset of Figure 3. The small amount of Ni-rich oxide, which we attributed to Ni_6MnO_8 is present as shown in inset XRD from 30 to 50. Figure 4 shows further analysis of the XRD patterns of LMNTO recorded using $\text{Cr K}\alpha$ ($2.29\ \text{\AA}$) instead of $\text{Cu K}\alpha$ as it is highly absorbed and poorly scattered by Mn. It can be seen that the lattice parameter, a , of the unsubstituted LMNO increases linearly with increasing Ti content (up to 0.3); from $8.168\ \text{\AA}$ to $8.197\ \text{\AA}$ due to the higher ionic radius of Ti^{4+} ($0.745\ \text{\AA}$) which is much larger than that of Mn^{4+} ($0.67\ \text{\AA}$) [27]. This monotonic increase in lattice parameter is in line with Vegard's law and could indicate that Ti^{4+} ions are incorporated into the lattice sites of the spinel structure as a solid solution and not on the grain boundaries.

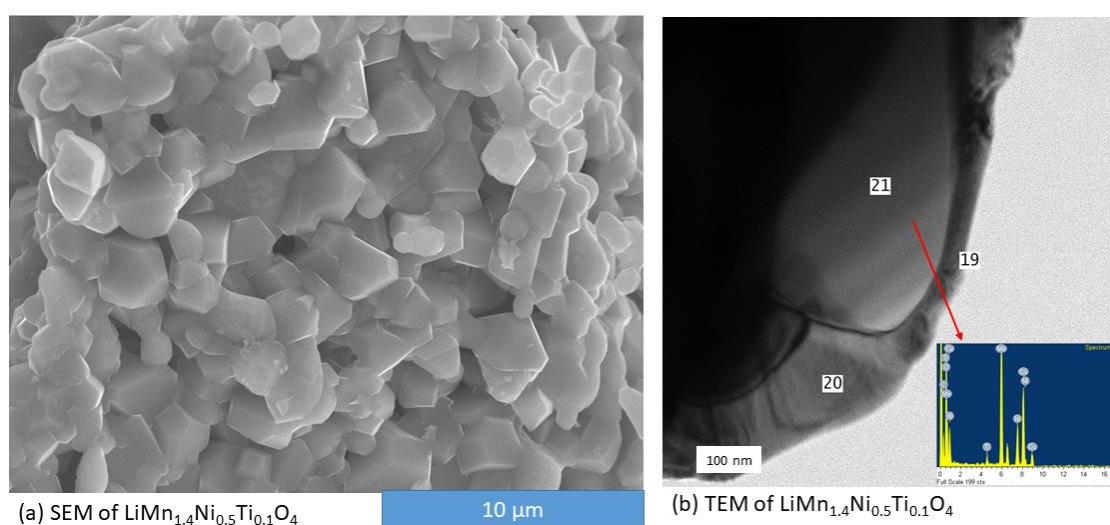


Figure 2. (a) SEM image and (b) TEM image and (inset) EDX of synthesized $\text{LMn}_{1.5-x}\text{Ni}_{0.5}\text{Ti}_x\text{O}$ ($x = 0.1$) material.

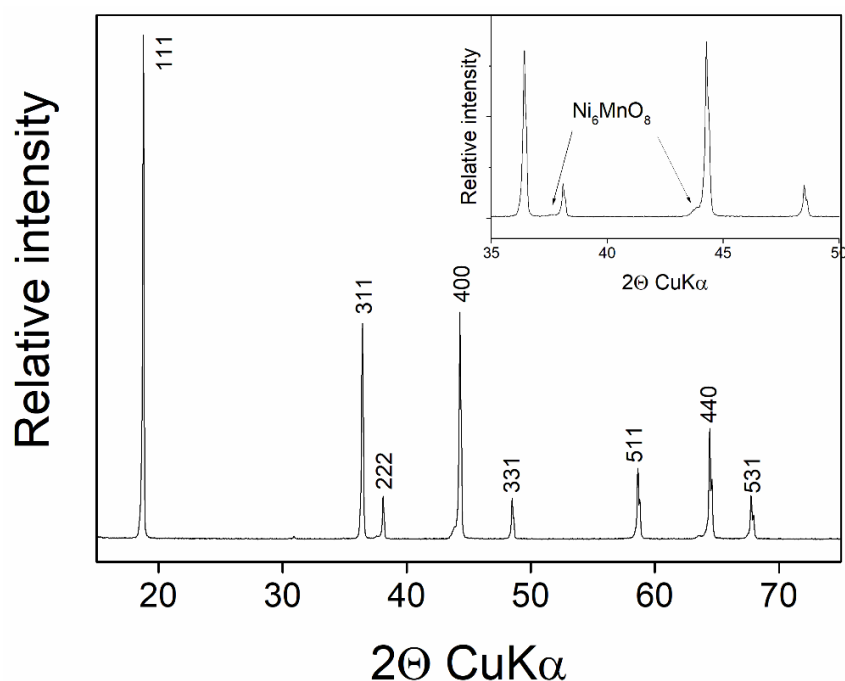


Figure 3. XRD pattern of synthesized LMNTO material.

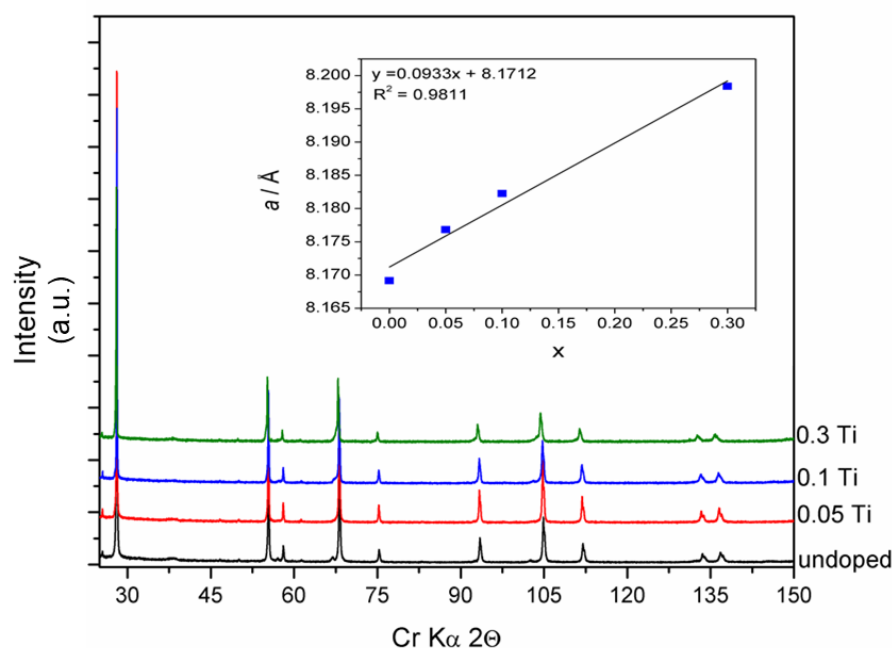


Figure 4. XRD patterns of synthesized LMNTO materials. Inset shows changes in lattice parameters as a function of substitution level.

To obtain more insight on the effect of Ti^{4+} ion on the chemical structure of LMNO, delithiated (50%) $\text{LiMn}_{1.4}\text{Ni}_{0.5}\text{Ti}_{0.1}\text{O}_4$ was studied both in the bulk and at the surface by synchrotron X-ray microscopies at Ti L-edge, Ni L3- and oxygen K-edge. Figures 5 and 6 show the chemical mapping of the particles and XANES from the surface and bulk of LMNTO particles. Two types of particles are present in these images, i.e., small particles such as the particles with a label of 1, and large particles such as the particles with a label of 2 as shown in the morphology image in Figure 5a. It can be revealed from the morphology mapping that both types of particles show well-defined shapes, which corresponds to typical spinel morphologies, namely octahedral shapes with (111) facets. The principal component analysis, PCA, shows different chemical components between the surface (purple) and bulk (green) of the large particle and between large (green) and small particles (labelled as particle 1). The detailed chemistry in those components can be further studied and compared by Ti L-edge XANES (Figure 5c) and Ni L3 edge XANES (Figure 5d) and O K-edge XANES (Figure 6). Ti L-edge XANES of all components presents the same spinel profile [34] which indicates uniform doping in LMNO spinel. The relative peak intensity at ~ 853 eV and 855 eV in Ni L3 edge XANES can be used to determine the Ni oxidation state [35] and the higher the second peak the higher the Ni oxidation state will be. The bulk in the large particle has a higher oxidation state, while the surface of the large bulk particles and the small particles has a lower Ni oxidation state. The variations can be related to LMNTO surface reactions with the electrolyte [35]. Figure 6 shows the O K-edge, XANES of delithiated $\text{LiMn}_{1.4}\text{Ni}_{0.5}\text{Ti}_{0.1}\text{O}_4$ extracted from STXM. Rich chemical variation among different components can be revealed by the obvious difference in their O K-edge XANES. The sharp peaks a and b are due to electron transition into O 2p hybridized with transition metal 3d orbitals. The relatively broad peaks c and d are due to the electron transition to the O 2p-transition metal 4sp state. The spectroscopic profile of the small particles resembles the spinel LMNO [36] and agrees with the Ni L3 edge XANES shown in Figure 5c. The merge of peaks c and d in the bulk of large $\text{LiMn}_{1.4}\text{Ni}_{0.5}\text{Ti}_{0.1}\text{O}_4$ is expected and agrees with the higher Ni oxidation state due to the delithiation. However, the enhanced b (529.5 eV) and c' (535.3 eV) peaks in the bulk of large particles and enhanced b in the surface of large particles is unexpected which is not observed in LNMO as reported by Zhou et al. [36] It must be related to Ti ion doping in the current sample and may be related to oxygen deficiency or oxygen redox activity. This may hint at a unique charge compensation mechanism in

$\text{LiMn}_{1.4}\text{Ni}_{0.5}\text{Ti}_{0.1}\text{O}_4$, being similar to that in TiO_2 lithiation [37], which warrants further XANES investigation. It should be noted that the well-reserved peaks c (536.2 eV) and d (543.8 eV) at the surface of large particles indicate a well-reserved spinel structure which could be related to a longer cycle life.

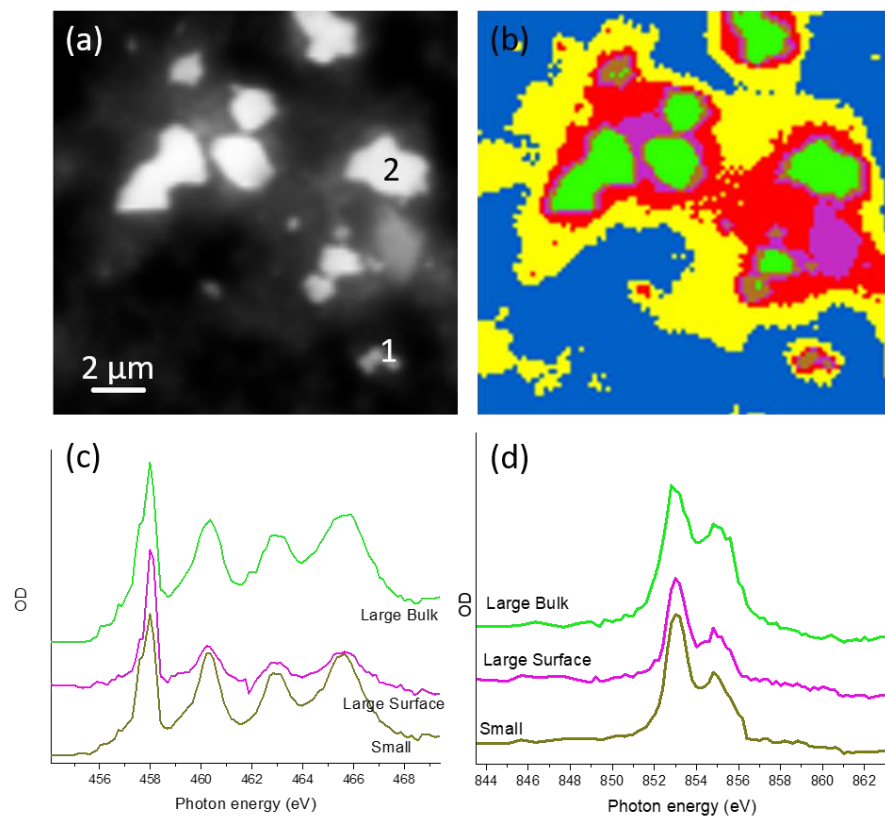


Figure 5. (a) Morphology mapping of $\text{LiMn}_{1.4}\text{Ni}_{0.5}\text{Ti}_{0.1}\text{O}_4$ particles, (b) components distribution mapping through principal component analysis (PCA), (c) Ti L3 XANES and (d) Ni L3 XANES of major components as shown in (b) (same color code is applied in (b–d)).

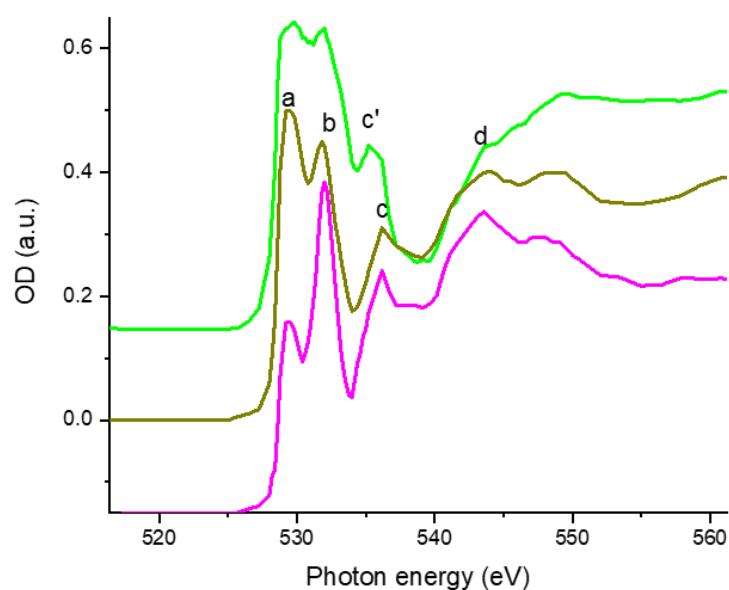


Figure 6. O K-edge XANES of the surface and bulk of large particles and small particles of $\text{LiMn}_{1.4}\text{Ni}_{0.5}\text{Ti}_{0.1}\text{O}_4$ from Figure 5.

4. Battery Results

4.1. Half-Cell Testing LMNTO vs. LMNO

Figure 7 shows the half-cell cycling behavior of $\text{LiMn}_{1.4}\text{Ni}_{0.5}\text{Ti}_{0.1}\text{O}_4$ and $\text{LiMn}_{1.5}\text{Ni}_{0.5}\text{O}_4$ and both materials showed excellent long-term cycling performance. Both materials have been cycled at room temperature and a C-rate of 2.22C for 2000 cycles. The discharge capacity of the LMNTO at the given rate was 123 mAh/g that is 15 mAh/g higher than LMNO, 108 mAh/g. Both materials showed a 17% loss of capacity at the end of 2000 cycles with 99% coulombic efficiencies. LMNTO loses capacity slowly over 2000 cycles, whereas LMNO loses most of the capacity at the first 500 cycles and stabilize at 90 mAh/g for the rest of the cycles.

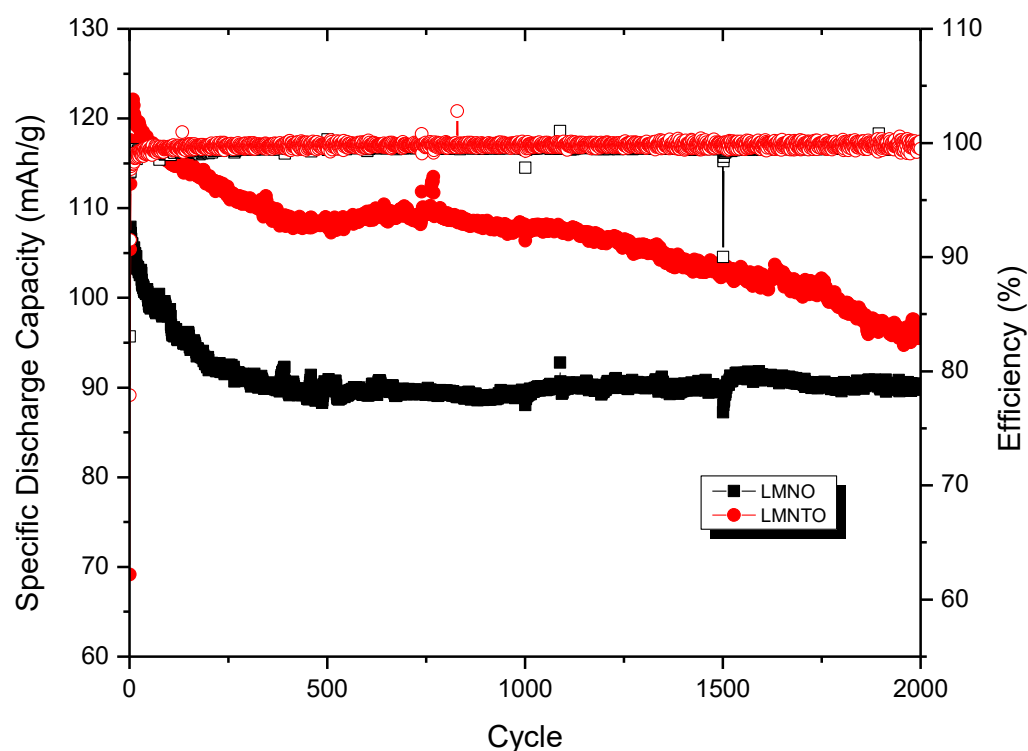


Figure 7. Cycling performance of LMNTO vs. LMNO materials in half cells showing specific discharge capacity for 2000 cycles.

Figure 8a shows the charge/discharge curves for initial cycles of $\text{LiMn}_{1.4}\text{Ni}_{0.5}\text{Ti}_{0.1}\text{O}_4$ cathode material. It is apparent that there is no 4 V plateau normally visible in the charge/discharge curves of Ni-deficient LMNO due to the absence of Mn^{3+} as the nickel content is closer to the ideal value of 0.5. It also shows that substitution with 0.1 Ti increases capacity by 20–30 mAh/g. However, this is accompanied by an increase in the irreversible capacity loss compared to unsubstituted $\text{LiMn}_{1.5}\text{Ni}_{0.5}\text{O}_4$. The curves of the initial cycles of $\text{LiMn}_{1.5}\text{Ni}_{0.5}\text{O}_4$ cathode material are also shown in Figure 8b. This has no 4 V plateau normally visible in the charge/discharge curves of Ni-deficient LMNO; as the nickel content is closer to the ideal value of 0.5. However, the plateau gaps between the charge and discharge were greater for Ni-deficient LMNO, 0.1 V which can be better seen from dQ/dV in Figure 8c,d. This will cause lower efficiency overall. Moreover, the result suggests LMNTO has a lower impedance than results on higher performance.

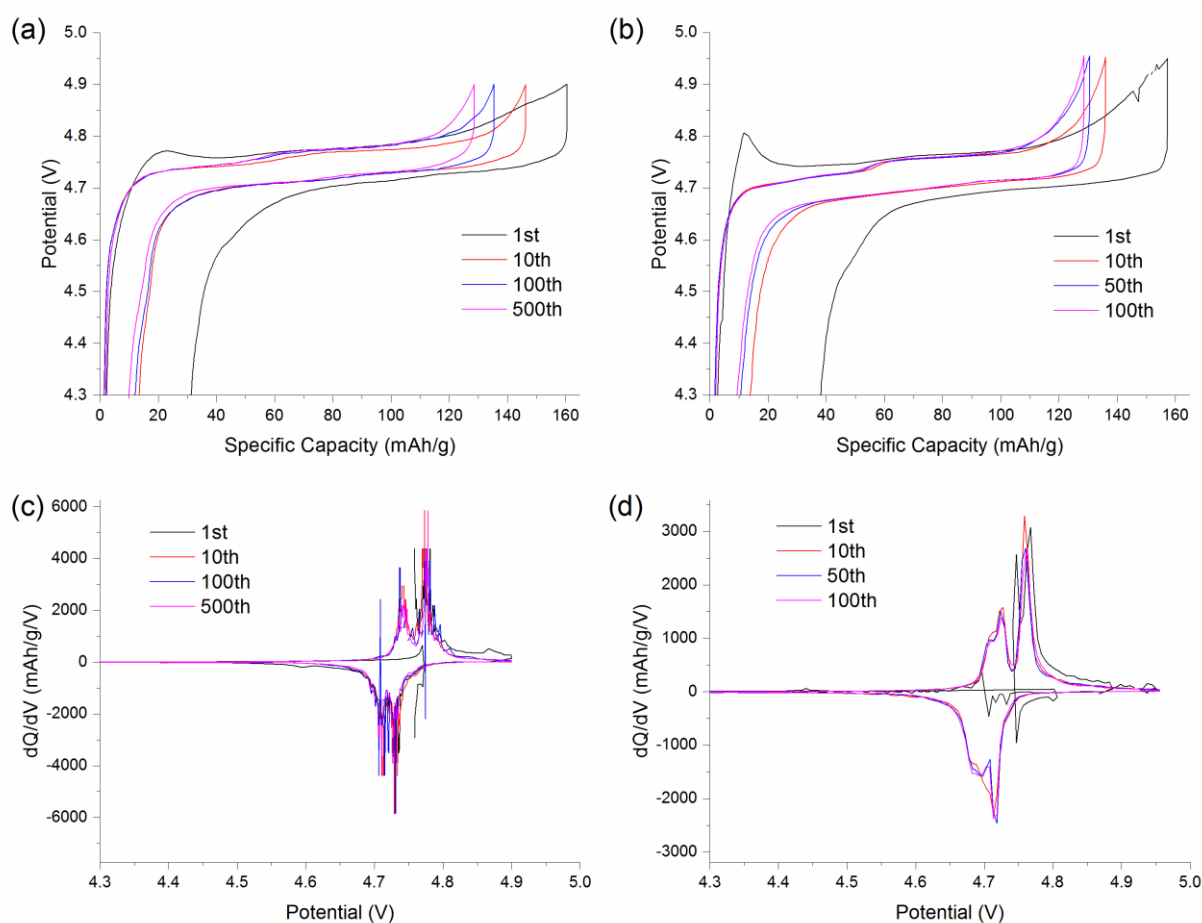


Figure 8. Charge/discharge and dQ/dV curves for LMNTO (a,c) and LMNO (b,d) materials.

The dQ/dV plot for the data is replotted in Figure 8c. In addition to clearly demonstrating the lack of redox behavior in the 4 V region, it shows that the redox behavior at 4.7 V is still split up to 100 cycles. It also shows good capacity retention up to 500 cycles with little change in voltage profile or capacity after the 100th cycle. A notable change in dQ/dV vs. V plot from 1st cycle to later cycles is observed, which may be the indication of a formation reaction occurring on 1st cycle that is distinguished in discharge profile. Clear resolution of the Ni²⁺ to Ni³⁺ and Ni³⁺ to Ni⁴⁺ steps in dQ/dV could be seen up to 500 cycles for LMNTO while the resolution retains at 100 cycles for LMNO, which is shown in Figure 8c,d.

To study the influence of C-rate and temperature on battery performance, LMNTO and LMNO were tested at different C-rates and temperatures as shown in Figure 9. It can be seen that for both room temperature and 60 °C higher C-rate, up to 10C, reduces the capacity and the capacity recovers back when C-rate was lowered back to C/2. The specific discharge capacity of LMNO were 102, 93, 74, 36 and 4 mAh/g at C/2, 1C, 2C, 5C and 10C, respectively, and for LMNTO were 110, 101, 86, 50 and 10 mAh/g at C/2, 1C, 2C, 5C and 10C, respectively. At 60 °C, the capacity was higher than the room temperature one for all C-rates, however, the coulombic efficiency was lower, 98% for room temperature and 89% for 60 °C, respectively.

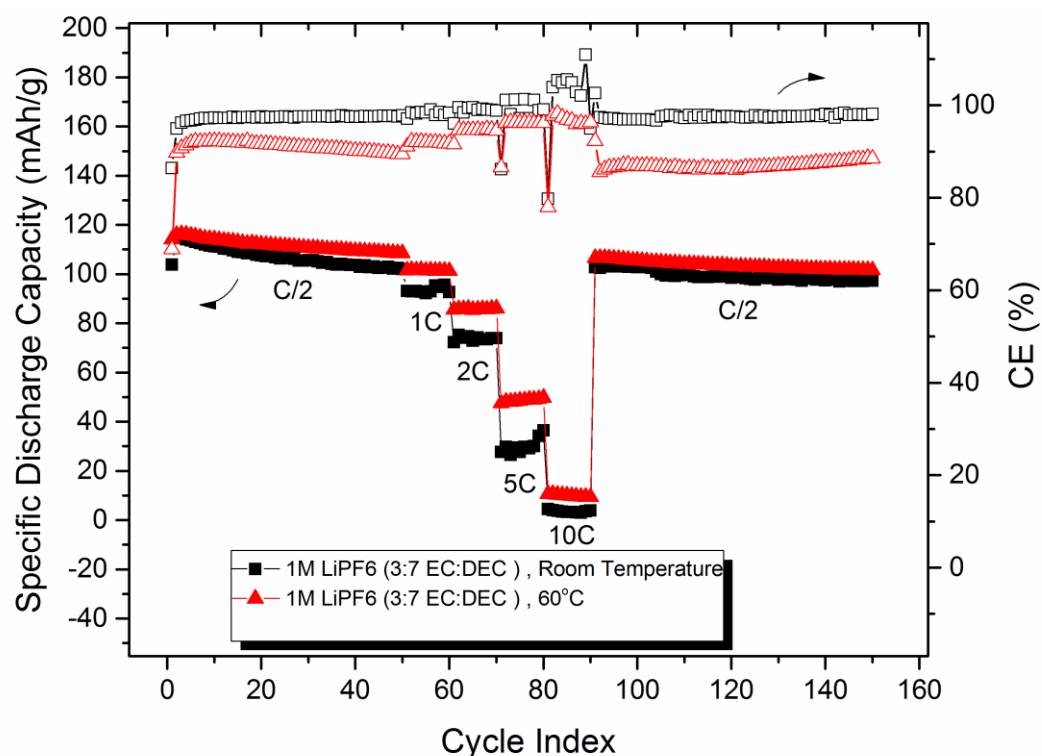


Figure 9. C-rate testing of LMNTO at room temperature and 60 °C.

4.2. AC Impedance of $\text{Li}/\text{LiNi}_{0.5}\text{Mn}_{1.4}\text{Ti}_{0.1}\text{O}_4$ Half Cells

Figure 10 shows the AC impedance plots of $\text{Li}/\text{LiNi}_{0.5}\text{Mn}_{1.4}\text{Ti}_{0.1}\text{O}_4$ half-cell at end of charge (4.8 V) and discharge (3.8 V) at room temperature (RT) and 60 °C. The bulk impedance is greater at the end of discharge (EOD) than at the end of charge (EOC). The impedance after EOC at RT stopped decreasing from 2112 $\Omega \text{ cm}^2$ at the first cycle to 314 $\Omega \text{ cm}^2$ at the 7th cycle, which might suggest stabilization of the cathode electrolyte interface (CEI) layer at the surface of LMNTO. However, the impedance after EOD continues to decrease after the 5th cycle from 213 $\Omega \text{ cm}^2$ to 118 $\Omega \text{ cm}^2$ at the 7th cycle. At 60 °C, the impedance at both EOC and EOD increased from 806 to 1753 $\Omega \text{ cm}^2$ for EOC and 671 to 1774 $\Omega \text{ cm}^2$ for EOD. At 60 °C, impedance after EOC was greater than the room temperature one that suggests the build-up of the CEI and reduction in the Li^+ ion kinetics. It is interesting to find that, even with the slower kinetics the specific capacity obtained from C-rate testing has shown higher specific capacity though with low efficiency at 60 °C compared to room temperature which could be attributed to an excess of lithium ions at the CEI layer.

4.3. Full-Cell Testing of LMNTO Cathode with Li Metal and $\text{Li}_4\text{Ti}_5\text{O}_{12}$ Anodes Battery Cycling of $\text{Li}_4\text{Ti}_5\text{O}_{12}/\text{LiNi}_{0.5}\text{Mn}_{1.4}\text{Ti}_{0.1}\text{O}_4$ Full Cells

Combining $\text{LiNi}_{0.5}\text{Mn}_{1.4}\text{Ti}_{0.1}\text{O}_4$ with $\text{Li}_4\text{Ti}_5\text{O}_{12}$ provides a cell with >3 V output with improved safety characteristics. However, the capacity of $\text{Li}_4\text{Ti}_5\text{O}_{12}/\text{LiNi}_{0.5}\text{Mn}_{1.4}\text{Ti}_{0.1}\text{O}_4$ cells degrades if charged to voltages > 3.5 V. The observation of any plateau above 3.5 V is evidence of electrolyte decomposition.

The cycling capabilities of the stoichiometric $\text{LiMn}_{1.5}\text{Ni}_{0.5}\text{O}_4$ cathodes vs. lithium metal and $\text{Li}_4\text{Ti}_5\text{O}_{12}$ anodes at a low 0.16C (22 mA/g) rate are shown in Figure 11. The initial discharge capacities were 115 and 136 mAh/g with the lithium and $\text{Li}_4\text{Ti}_5\text{O}_{12}$ anode, respectively. The capacity retention was 91% with Li metal anode for 100 cycles and 94% with $\text{Li}_4\text{Ti}_5\text{O}_{12}$ anode for over 60 cycles. Closer examination of first cycle voltage vs. capacity of the same cells revealed that 1st cycle irreversibility in the $\text{Li}_4\text{Ti}_5\text{O}_{12}$ anode was reduced to less than 14 mAh/g, even though the cell operated over the 3 V plateau. All

coin cell tests were performed without any modifications of initially synthesized LMNO and LMNTO powder materials or optimizations in terms of the composition of materials, coating of particles, pore size adjustments, thicknesses, etc. The same applied to LTO Anodes in full-coin cells arrangements. Further improvements need to be performed in selecting optimal electrolyte compositions and additives designed for high-rate, high-voltage cathode materials in Li-ion rechargeable batteries.

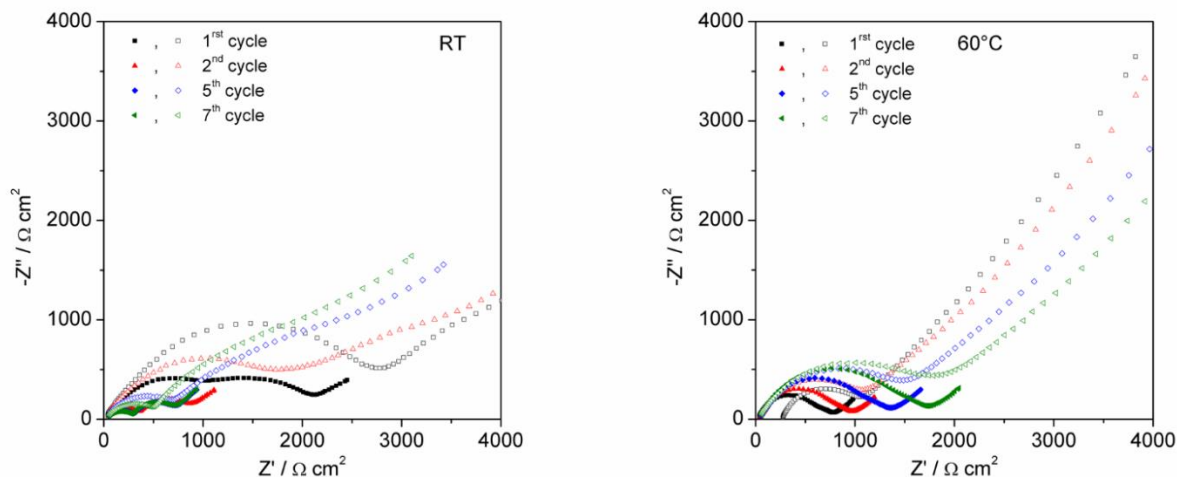


Figure 10. EIS of LMNTO at room temperature and 60 °C. Filled signs marked EOC, empty marked EOD.

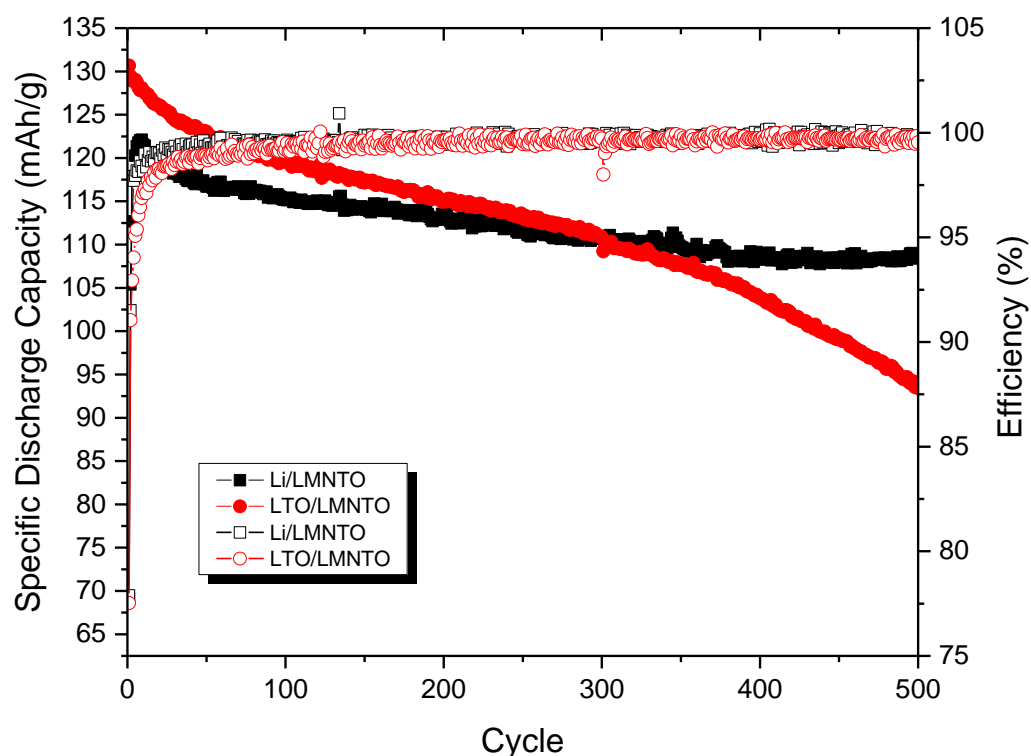


Figure 11. Cycling performance of LMNTO material in half and full cells with LTO showing specific discharge capacity for 500 cycles.

5. Conclusions

High voltage $\text{LiMn}_{1.5}\text{Ni}_{0.5}\text{O}_4$ and $\text{LiNi}_{0.5}\text{Mn}_{1.5-x}\text{Ti}_x\text{O}_4$ ($x = 0.05, 0.1, 0.3$) cathode materials that suffer from two grand limitations, long term cycling stability and high-temperature performance in conventional carbonate-based electrolytes, were synthesized

by a sol-gel method, characterized and their electrochemical properties and battery performance were studied. It was demonstrated that partial substitution of Mn with Ti resolves the long-term cycling limitation with this type of materials and galvanostatic cycling over 2000 cycles was shown and was proven to be a result of a possible charge compensation mechanism as evidenced by a Soft X-ray Spectromicroscopy study of delithiated LM-NTO materials. However, it does not resolve the second limitation of electrochemical performance at elevated temperatures with conventional electrolytes, but careful choice of electrolyte formulation has the potential to overcome this limitation and render these materials suitable for high energy density lithium batteries.

Author Contributions: Conceptualization, C.-H.Y. and Y.A.-L.; methodology, S.N.; software, C.-H.Y.; validation, Y.A.-L.; formal analysis, C.-H.Y., J.W. and Y.A.-L.; investigation, S.N. and J.Z.; resources, S.N.; data curation, C.-H.Y.; writing—original draft preparation, C.-H.Y.; writing—review and editing, Y.A.-L.; visualization, Y.A.-L.; supervision, Y.A.-L.; project administration, Y.A.-L.; funding acquisition, Y.A.-L. All authors have read and agreed to the published version of the manuscript.

Funding: This research received no external funding.

Institutional Review Board Statement: Not applicable.

Informed Consent Statement: Not applicable.

Acknowledgments: The authors would like to thank Natural Resources Canada for financial support through the Office of Energy Research and Development. The authors would like to extend thanks to Pamela Whitfield for her help in the X-ray diffraction characterization of the materials and Hugues Duncan for his help in the EIS measurements. The authors acknowledge extra support from the Canadian Light Source, a national research facility of the University of Saskatchewan, supported by the Canada Foundation for Innovation (CFI), the Natural Sciences and Engineering Research Council (NSERC), the National Research Council (NRC), the Canadian Institutes of Health Research (CIHR), the Government of Saskatchewan, and the University of Saskatchewan.

Conflicts of Interest: The authors declare no conflict of interest.

References

1. Amine, K.; Tukamoto, H.; Yasuda, H.; Fujita, Y. A new three-volt spinel $\text{Li}_{1+x}\text{Mn}_{1.5}\text{Ni}_{0.5}\text{O}_4$ for secondary lithium batteries. *J. Electrochem. Soc.* **1996**, *143*, 1607–1613. [[CrossRef](#)]
2. Caballero, A.; Cruz, M.; Hernán, L.; Melero, M.; Morales, J.; Castellón, E.R. Nanocrystalline materials obtained by using a simple, rapid method for rechargeable lithium batteries. *J. Power Sources* **2005**, *150*, 192–201. [[CrossRef](#)]
3. Park, S.B.; Eom, W.S.; Cho, W.I.; Jang, H. Electrochemical properties of $\text{LiNi}_{0.5}\text{Mn}_{1.5}\text{O}_4$ cathode after Cr doping. *J. Power Sources* **2006**, *159*, 679–684. [[CrossRef](#)]
4. Ein-Eli, Y.; Urian, R.C.; Wen, W.; Mukerjee, S. Low temperature performance of copper/nickel modified LiMn_2O_4 spinels. *Electrochim. Acta* **2005**, *50*, 1931–1937. [[CrossRef](#)]
5. Wei, Y.; Nam, K.W.; Kim, K.B.; Chen, G. Spectroscopic studies of the structural properties of Ni substituted spinel LiMn_2O_4 . *Solid State Ion.* **2006**, *177*, 29–35. [[CrossRef](#)]
6. Kunduraci, M.; Amatucci, G.G. Effect of oxygen non-stoichiometry and temperature on cation ordering in $\text{LiMn}_{2-x}\text{Ni}_x\text{O}_4$ ($0.50 \geq x \geq 0.36$) spinels. *J. Power Sources* **2007**, *165*, 359–367. [[CrossRef](#)]
7. Arunkumar, T.A.; Manthiram, A. Influence of chromium doping on the electrochemical performance of the 5 V spinel cathode $\text{LiMn}_{1.5}\text{Ni}_{0.5}\text{O}_4$. *Electrochim. Acta* **2005**, *50*, 5568–5572. [[CrossRef](#)]
8. Wu, X.; Kim, S.B. Improvement of electrochemical properties of $\text{LiNi}_{0.5}\text{Mn}_{1.5}\text{O}_4$ spinel. *J. Power Sources* **2002**, *109*, 53–57. [[CrossRef](#)]
9. Zhong, Q.; Bonakdarpour, A.; Zhang, M.; Gao, Y.; Dahn, J.R. Synthesis and Electrochemistry of $\text{LiNi}_x\text{Mn}_{2-x}\text{O}_4$. *J. Electrochem. Soc.* **1997**, *144*, 205–213. [[CrossRef](#)]
10. Dokko, K.; Mohamedi, M.; Anzue, N.; Itoh, T.; Uchida, I. In situ Raman spectroscopic studies of $\text{LiNi}_x\text{Mn}_{2-x}\text{O}_4$ thin film cathode materials for lithium ion secondary batteries. *J. Mater. Chem.* **2002**, *12*, 3688–3693. [[CrossRef](#)]
11. Liu, G.Q.; Wang, Y.J.; Li, W. Synthesis and electrochemical performance of $\text{LiNi}_{0.5}\text{Mn}_{1.5}\text{O}_4$ spinel compound. *Electrochim. Acta* **2005**, *50*, 1965–1968. [[CrossRef](#)]
12. Idemoto, Y.; Narai, H.; Koura, N. Crystal structure and cathode performance dependence on oxygen content of $\text{LiMn}_{1.5}\text{Ni}_{0.5}\text{O}_4$ as a cathode material for secondary lithium batteries. *J. Power Sources* **2003**, *119*, 125–129. [[CrossRef](#)]
13. Fang, H.; Li, L.; Li, G. A low-temperature reaction route to high rate and high capacity $\text{LiNi}_{0.5}\text{Mn}_{1.5}\text{O}_4$. *J. Power Sources* **2007**, *167*, 223–227. [[CrossRef](#)]

14. Kanamura, K.; Hoshikawa, W.; Umegaki, T. Electrochemical Characteristics of $\text{LiNi}_{0.5}\text{Mn}_{1.5}\text{O}_4$ Cathodes with Ti or Al Current Collectors. *J. Electrochem. Soc.* **2002**, *149*, A339–A345. [[CrossRef](#)]
15. Li, T.; Qiu, W.; Zhang, G.; Zhao, H.; Liu, J. Synthesis and electrochemical characterization of 5 V $\text{LiNi}_{1/2}\text{Mn}_{3/2}\text{O}_4$ cathode materials by low-heating solid-state reaction. *J. Power Sources* **2007**, *174*, 515–518. [[CrossRef](#)]
16. Lazarraga, M.G.; Pascual, L.; Gadjov, H.; Kovacheva, D.; Petrov, K.; Amarilla, J.M.; Rojas, R.M.; Martin-Luengo, M.A.; Rojo, J.M. Nanosize $\text{LiNi}_y\text{Mn}_{2-y}\text{O}_4$ ($0 < y \leq 0.5$) spinels synthesized by a sucrose-aided combustion method. Characterization and electrochemical performance. *J. Mater. Chem.* **2004**, *14*, 1640–1647. [[CrossRef](#)]
17. Amarilla, J.M.; Rojas, R.M.; Pico, F.; Pascual, L.; Petrov, K.; Kovacheva, D.; Lazarraga, M.G.; Lejona, I.; Rojo, J.M. Nanosized $\text{LiM}_y\text{Mn}_{2-y}\text{O}_4$ ($M = \text{Cr, Co and Ni}$) spinels synthesized by a sucrose-aided combustion method: Structural characterization and electrochemical properties. *J. Power Sources* **2007**, *174*, 1212–1217. [[CrossRef](#)]
18. Olejniczak, A.B.; Corsini, M.; Fedi, S.; Zanello, P.; Lesnikowski, Z.J. Nucleoside–metallacarborane conjugates for multipotential electrochemical coding of DNA. *Electrochem. Commun.* **2007**, *9*, 1007–1011. [[CrossRef](#)]
19. Kim, J.H.; Myung, S.T.; Sun, Y.K. Molten salt synthesis of $\text{LiNi}_{0.5}\text{Mn}_{1.5}\text{O}_4$ spinel for 5 V class cathode material of Li-ion secondary battery. *Electrochim. Acta* **2004**, *49*, 219–227. [[CrossRef](#)]
20. Park, S.-H.; Sun, Y.-K. Synthesis and electrochemical properties of 5 V spinel $\text{LiNi}_{0.5}\text{Mn}_{1.5}\text{O}_4$ cathode materials prepared by ultrasonic spray pyrolysis method. *Electrochim. Acta* **2004**, *50*, 431–434. [[CrossRef](#)]
21. Kang, S.-H.; Goodenough, J.B.; Rabenberg, L.K. Nanocrystalline Lithium Manganese Oxide Spinel Cathode for Rechargeable Lithium Batteries. *Electrochem. Solid-State Lett.* **2001**, *4*, A49–A51. [[CrossRef](#)]
22. Yi, T.-F.; Hu, X.-G. Preparation and characterization of sub-micro $\text{LiNi}_{0.5-x}\text{Mn}_{1.5+x}\text{O}_4$ for 5 V cathode materials synthesized by an ultrasonic-assisted co-precipitation method. *J. Power Sources* **2007**, *167*, 185–191. [[CrossRef](#)]
23. Kunduraci, M.; Al-Sharab, J.F.; Amatucci, G.G. High-Power Nanostructured $\text{LiMn}_{2-x}\text{Ni}_x\text{O}_4$ High-Voltage Lithium-Ion Battery Electrode Materials: Electrochemical Impact of Electronic Conductivity and Morphology. *Chem. Mater.* **2006**, *18*, 3585–3592. [[CrossRef](#)]
24. Kelder, E.M.; Ooms, F.J.B.; Perego, R.; Schoonman, J. $\text{Li}_{1+\delta}\text{Mn}_{2-\delta}\text{O}_4$ performance measured by leaching. *J. Power Sources* **2001**, *97*, 433–436. [[CrossRef](#)]
25. Kunduraci, M.; Amatucci, G.G. Synthesis and Characterization of Nanostructured 4.7 V $\text{Li}_x\text{Mn}_{1.5}\text{Ni}_{0.5}\text{O}_4$ Spinel for High-Power Lithium-Ion Batteries. *J. Electrochem. Soc.* **2006**, *153*, A1345–A1352. [[CrossRef](#)]
26. Niketic, S.; Couillard, M.; MacNeil, D.; Abu-Lebdeh, Y. Improving the performance of high voltage $\text{LiMn}_{1.5}\text{Ni}_{0.5}\text{O}_4$ cathode material by carbon coating. *J. Power Sources* **2014**, *271*, 285–290. [[CrossRef](#)]
27. Lin, M.; Wang, S.H.; Gong, Z.L.; Huang, X.K.; Yang, Y. A Strategy to Improve Cyclic Performance of $\text{LiNi}_{0.5}\text{Mn}_{1.5}\text{O}_4$ in a Wide Voltage Region by Ti-Doping. *J. Electrochem. Soc.* **2013**, *160*, A3036–A3040. [[CrossRef](#)]
28. Alcántara, R.; Jaraba, M.; Lavela, P.; Tirado, J.L.; Biensan, P.; de Guibert, A.; Jordy, C.; Peres, J.P. Structural and Electrochemical Study of New $\text{LiNi}_{0.5}\text{Ti}_x\text{Mn}_{1.5-x}\text{O}_4$ Spinel Oxides for 5 V Cathode Materials. *Chem. Mater.* **2003**, *15*, 2376–2382. [[CrossRef](#)]
29. Jin, Y.-Z.; Lv, Y.-Z.; Xue, Y.; Wu, J.; Zhang, X.-G.; Wang, Z.-B. Improved electrochemical performance of $\text{LiNi}_{0.4}\text{Ti}_{0.1}\text{Mn}_{1.5}\text{O}_4$ as cathode of lithium ion battery by carbon-coating. *RSC Adv.* **2014**, *4*, 57041–57047. [[CrossRef](#)]
30. Kim, J.-H.; Pieczonka, N.P.W.; Sun, Y.-K.; Powell, B.R. Improved lithium-ion battery performance of $\text{LiNi}_{0.5}\text{Mn}_{1.5-x}\text{Ti}_x\text{O}_4$ high voltage spinel in full-cells paired with graphite and $\text{Li}_4\text{Ti}_5\text{O}_{12}$ negative electrodes. *J. Power Sources* **2014**, *262*, 62–71. [[CrossRef](#)]
31. Höweling, A.; Glatthaar, S.; Nötzel, D.; Binder, J.R. Evidence of loss of active lithium in titanium-doped $\text{LiNi}_{0.5}\text{Mn}_{1.5}\text{O}_4$ /graphite cells. *J. Power Sources* **2015**, *274*, 1267–1275. [[CrossRef](#)]
32. Pawley, G. Unit-cell refinement from powder diffraction scans. *J. Appl. Crystallogr.* **1981**, *14*, 357–361. [[CrossRef](#)]
33. Rietveld, H. Line profiles of neutron powder-diffraction peaks for structure refinement. *Acta Crystallogr.* **1967**, *22*, 151–152. [[CrossRef](#)]
34. Uceda, M.; Zhou, J.; Wang, J.; Gauvin, R.; Zaghbi, K.; Demopoulos, G.P. Highly conductive NMP-free carbon-coated nano-lithium titanate/carbon composite electrodes via SBR-assisted electrophoretic deposition. *Electrochim. Acta* **2019**, *299*, 107–115. [[CrossRef](#)]
35. Lu, M.; Wang, J.; Fang, H.; Hu, Y.; Zhou, J. Unexpected phase separation in $\text{Li}_{1-x}\text{Ni}_{0.5}\text{Mn}_{1.5}\text{O}_4$ within a porous composite electrode. *Chem. Commun.* **2018**, *54*, 4152–4155. [[CrossRef](#)]
36. Zhou, J.; Hong, D.; Wang, J.; Hu, Y.; Xie, X.; Fang, H. Electronic structure variation of the surface and bulk of a $\text{LiNi}_{0.5}\text{Mn}_{1.5}\text{O}_4$ cathode as a function of state of charge: X-ray absorption spectroscopic study. *Phys. Chem. Chem. Phys.* **2014**, *16*, 13838–13842. [[CrossRef](#)] [[PubMed](#)]
37. Zhou, J.; Fang, H.; Maley, J.; Murphy, M.; Ko, J.P.; Cutler, J.; Sammynaiken, R.; Sham, T.; Liu, M.; Li, F. Electronic structure of TiO_2 nanotube arrays from X-ray absorption near edge structure studies. *J. Mater. Chem.* **2009**, *19*, 6804–6809. [[CrossRef](#)]